ACS Catalysis

Open Access

pubs.acs.org/acscatalysis

Research Article

Identifying Reactive Trends in Glycerol Electro-Oxidation Using an Automated Screening Approach: 28 Ways to Electrodeposit an Au Electrocatalyst

Raghuram Gaddam, Zirui Wang, Yichen Li, Lauren C. Harris, Michael A. Pence, Efren R. Guerrero, Paul J. A. Kenis, Andrew A. Gewirth, and Joaquín Rodríguez-López*

Cite This: *ACS Catal.* 2025, 15, 639−652

Read Online

ACCESS | Metrics & More | Article Recommendations | Supporting Information

ABSTRACT: Automated, rapid electrocatalyst discovery techniques that comprehensively address the exploration of chemical spaces, characterization of catalyst robustness, reproducibility, and translation of results to (flow) electrolysis operation are needed. Responding to the growing interest in biomass valorization, we studied the glycerol electro-oxidation reaction (GEOR) on gold in alkaline media as a model reaction to demonstrate the efficacy of such methodology introduced here. Our platform combines individually addressable electrode arrays with HardPotato, a Python application programming interface for potentiostat control, to automate electrochemical experiments and data analysis operations. We systematically investigated the effects of reduction potential (E_l) and pulse width (PW) on GEOR activity during the electrodeposition (Edep) of gold, evaluating 28 different conditions in triplicate measurements with great versatility. Our findings reveal a direct correlation between E_l and GEOR activity. Upon CV cycling, we recorded a 52% increase in peak current density and a −0.25 V shift in peak potential as E_l varied from −0.2 to −1.4 V. We also identified an optimal PW of ∼1.0 s, yielding maximum catalytic performance. The swift analysis enabled by our methodology allowed us to correlate performance enhancements with increased electrochemical surface area and preferential deposition of Au(110) and Au(111) sites, even in disparate Edep conditions. We validate our methodology by scaling the Edep process to larger electrodes and correlating intrinsic activity with product speciation via flow electrolysis measurements. Our platform highlights opportunities in automation for electrocatalyst discovery to address pressing needs toward industrial decarbonization, such as biomass valorization.

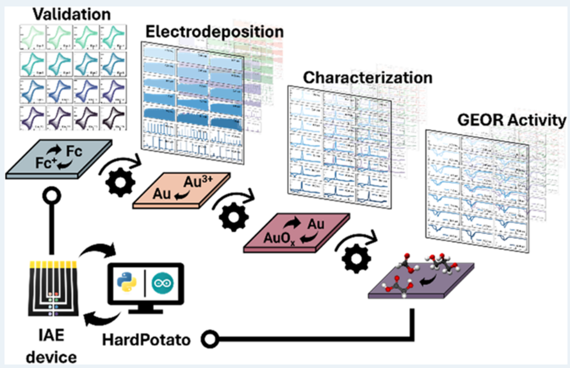

KEYWORDS: *pulse width, reduction potential, catalytic performance, GEOR activity*

■ INTRODUCTION

Electrochemical valorization of biomass has emerged as a promising approach to furthering the global initiative of electrifying the chemical industry. This approach allows transitioning away from fossil-fuel-based processes and toward more sustainable and carbon-neutral technologies for chemical and fuel production.[1−4] Among the host of biomass molecules available, glycerol, a byproduct from soap production and the burgeoning biodiesel industry[5] holds particular interest due to its affordability ($0.3/kg) and nontoxicity. The oxidation of glycerol's hydroxyl groups via the glycerol electro-oxidation reaction (GEOR) is reported to yield a plethora of value-added products[1,6,7] such as tartronic acid ($467/kg),[8] mesoxalic acid ($1400/kg),[9] and glyceric acid ($2100/kg)[10] as well as industrially significant chemicals such as formic acid,[1] glycolic acid,[11] and oxalic acid.[12]

Moreover, GEOR also serves as a financially viable and energy-efficient alternative to the oxygen evolution reaction (OER),[13−16] conventionally occurring at the anode of CO_2 reduction reaction (CO_2RR) and hydrogen evolution reaction (HER) electrolyzer cells. OER, a complex four-electron transfer process, is both energetically intensive and unprofitable due to its main byproduct−O_2,[17−19] which has limited market value. The theoretical overpotential OER is 1.23 V vs RHE, yet in practice, it requires >1.8 V to drive the reaction owing to sluggish kinetics.[20] Verma et al.[16] reported that substituting OER with GEOR in a CO_2RR electrolyzer lowers electricity consumption by 53%. Similarly, Qian et al.[21] achieved a 10% reduction in energy consumption while

Received: July 14, 2024
Accepted: November 7, 2024
Published: December 23, 2024

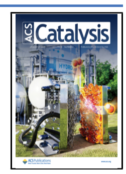

operating an H_2 production electrolyzer at industrial-level current densities simply by substituting OER with GEOR.

Building on the demonstrated advantages of the GEOR as a compelling option for modern energy strategies, we hypothesized that its efficiency could be further augmented by exploring metallic electrocatalysts. Despite numerous catalyst design strategies aimed at increasing the number of active sites and enhancing intrinsic activity,[3,22] the field suffers from fragmented research and a lack of comprehensive methodologies for catalyst evaluation, with trial and error still prevailing as the guiding principle for catalyst discovery. Furthermore, discrepancies in reported performances often arise from variations in experimental conditions such as mass loading, analyte concentration, and pH, emphasizing the need for standardized electrocatalyst discovery and testing protocols.

Recognizing this, we posit a critical need for a rapid screening methodology to screen electrocatalysts. This approach would facilitate the creation of a comprehensive database and aid in predicting new materials.[23] Several high-throughput (HT) electrochemical (EChem) screening technologies have been proposed, most of which can be classified into three major categories—scanning probe techniques, indirect measurements using optical/spectroscopic signals, and direct current/voltage measurements.[24] A few of these techniques are summarized below.

Scanning probe methods such as scanning electrochemical microscopy (SECM) have been proposed to screen catalysts for reactions such as CO_2 reduction,[25] oxygen reduction and hydrogen oxidation,[26] oxygen evolution,[27] and formic acid oxidation.[28] While quite powerful and information-rich, SECM-based screening methods primarily involve local delivery of species to electrodes via electro-generation, which complicates the screening possibilities for alcohol oxidation reactions. Additionally, they often require elaborate sample preparation steps that involve piezoelectric dispensing of metal salt solutions followed by reduction at elevated temperatures.[26] This provides poor control over surface structure and morphology and is plagued by further complications during synthesis scale-up from microscale to practical-scale cell setups.

pH imaging screening methodologies have also been reported for the evaluation of electrocatalysts.[29] In such techniques, an electrochemical reaction at the surface of the electrode leads to a change in the local pH, which is imaged using a pH-sensitive fluorescence dye. However, such techniques are typically functional only in a narrow pH window.[30] Similarly, Xiang et al.[30] report an electrocatalyst screening technique in which bubble evolution is mapped as a function of activity; however, this method's scope is restricted to reactions involving gas evolution. While these screening techniques are rapid, most rely on indirect indicators for catalytic performance and suffer from crosstalk from materials due to the overlap of diffusional fields from adjacent electrodes.[24] Another avenue recently explored for enabling HT electrochemical screening involves using microelectrode arrays for current and potential measurements.[31,32]

Considering the constraints posed by current screening architectures, we introduce a novel approach in this paper leveraging HardPotato, an open-source Python API recently developed by the Rodriguez-López group,[33,34] and individually addressable electrode (IAE) array devices. We demonstrate the applicability of this methodology to screen for the electrocatalytic performance of Au NPs exhibiting diverse physical properties. We accentuate the automatability of our approach by employing electrodeposition (Edep) as a versatile and cost-effective synthesis technique. Control over deposition parameters enables tuning features such as morphology, size, and composition, which is crucial for optimizing their electrocatalytic performance. We assessed the activity of different Au electrodeposits toward GEOR, driven by the reaction's immense economic and environmental benefits.[35] Although palladium is recognized for its high intrinsic activity for GEOR,[36] it is prone to surface passivation due to the early onset of oxide formation and adsorbed carbon monoxide (CO_{ads}) poisoning. In contrast, gold has been demonstrated to have higher CO_{ads} resistance and attain appreciably higher currents (>5×) than platinum and palladium, albeit at higher oxidation potentials.[37,38] Considering that GEOR involves the adsorption of various intermediates, we hypothesized that by tuning the Edep parameters of gold, we could adjust the catalyst surface properties, size, loading, and morphology, thereby influencing the adsorption energies of these intermediates as well as overall reactivity.[3]

Using our new methodology, we explored a total of 28 different electrodeposition parameter combinations and verified them through triplicate measurements to underscore the reproducibility of the technique. We established trendlines correlating the Edep parameters to the properties of Au active sites and their GEOR performance with minimal human intervention. The validity of our findings was further confirmed through flow-electrolysis experiments to test their scaling up, illustrating our methodology's applicability to advanced electrocatalysis studies.

MATERIALS AND METHODS

Chemicals and Materials. All materials were purchased and used as received. Sodium phosphate monobasic (NaH_2PO_4), sodium phosphate dibasic (Na_2HPO_4), potassium nitrate (KNO_3, 99+%), and tetrachloroauric(III) acid trihydrate trace metals basis ($HAuCl_4 \cdot 3H_2O$, 99.9%) were purchased from Sigma-Aldrich. Hydroxymethyl ferrocene (FcMeOH, 97%) was purchased from Alfa Aesar. Sulfuric acid (H_2SO_4, Trace metal grade), potassium hydroxide pellets (KOH, ACS reagent, 85%), glycerol (ACS reagent, 99.6%), and graphite rod (99.9995%) were purchased from Thermo Scientific. Ni foil (Trace Metal, 99.00%) was purchased from ChemDirect. All solutions were prepared using high-performance liquid chromatography-grade water.

Device Microfabrication. IAE array devices were fabricated on 4-in. glass wafers sourced from University Wafers, following a previously established workflow. Initially, the wafers were subjected to a degreasing process with acetone and isopropanol, followed by plasma treatment and RCA-1 cleaning. The metal layer for the electrodes and their circuitry was patterned by photolithography using an SPR 220−4.5/LOR 5A bilayer photoresist followed by the sputtering of gold (t = 180.0 s), with titanium (t = 60.0 s) as the adhesion layer, and liftoff performed with Microposit 1165 remover. After liftoff, the wafers were plasma and RCA-1 cleaned again, and a 1 μm thick SiO_2 insulating layer was deposited via plasma-enhanced chemical vapor deposition (PECVD). A KMPR photoresist layer was then photolithographically patterned to define the area for the electrodes and electrical connection. The exposed SiO_2 was then etched with a CF_4 plasma. After etching, the wafer was spin-coated with a protective SPR 220−4.5 photoresist layer for dicing and then diced into individual IAE devices by an electrical discharge machine. Prior to making the electrical connection, the devices were cleaned by degreasing and plasma treatment (under O_2 flow for 6 min). Since the devices were subjected to oxidative pretreatment, this led to the forming of an AuO_x layer over the surface of the electrodes, which was removed by electrochemical cleaning in a phosphate buffer solution (pH = 7).

Electrochemical Cell Assembly. Flex cables (Digi-Key, CA-DK05−12−30.0-A-44−88) were attached to the IAE devices by an anisotropic conductive film (3M, 3M970312-ND) followed by pressing under a manual heat press operated using a DC voltage supply set to 65−70 V, for 5.0 min. The IAE devices were then housed in a three-dimensional (3D) printed electrochemical cell sealed with an elastomer O-ring to avoid solution leaking. The cells were then connected to an 8−1 multiplexer powered by an Arduino Uno CPU using a printed circuit board adaptor (Meccanixity FPC FFC Converter Board 12P 0.5 mm). Electrochemical measurements were performed by employing a three-electrode setup and a CHI760 potentiostat as the electrochemical workstation. The electrode array on the IAE device was used as the working electrode (WE), and a graphite counter electrode (CE) was connected via Cu tape. All measurements were made using a lab-made Ag/AgCl (3 M KCl) reference electrode (RE). The RE was introduced into the solution using an agar-based salt bridge to avoid contamination of the experiment cell with Ag^+ ions.

Electrochemical Measurements. *Cleaning and Validation.* Electrochemical cleaning of bare Au electrodes was done in a 0.1 M phosphate buffer solution (pH = 7) by performing cyclic voltammetry (CV) measurements within the potential window of 0.2 to −1.5 V@0.1 V/s for 50 cycles. Before Edep, size validation studies were performed in 1.16 mM FcMeOH + 0.1 M KNO_3 on all electrode arrays reported in this study using CV measurements, which were recorded in the potential range of −0.1 − 0.5 V at scan rates in the range of 0.1−1.0 V/s (100 mV/s increments) for 5 cycles at each scan rate.

Electrodeposition of Au NPs. For pulsed electrodeposition (PED) of Au-NPs, 1.0 mM $HAuCl_4$ + 0.5 M H_2SO_4 was used as the precursor solution, while electrodeposition was performed at lower end potential (E_l) of −0.2, −0.6, −1.0, and −1.4 V (vs Ag/AgCl) and at pulse widths (PW) = 0.01, 0.05, 0.2, 1.0, 5.0, 30.0, and 60.0 s. The higher-end potential (E_h) was held at a constant potential of 1.0 V (vs Ag/AgCl), and the total Edep time was fixed at 5.0 min. As a result, the number of pulses applied were 60,000, 12,000, 3000, 600, 120, 20, and 10 for their corresponding PW.

Electrochemical Characterization of Au NPs. To estimate the ECSA, we performed CV cycling in 0.5 M H_2SO_4 within the potential window of −0.35 − 1.55 V@0.1 V/s for 10 cycles. The charge passed during the reduction of the gold oxide layer is calculated using Q_{red} = (area under peak/scan rate) and normalized using a factor of 390 $\mu C/cm^2$ for pure Au.[39]

Glycerol Electro-Oxidation Reaction (GEOR). Initially, the electrodes were conditioned by cycling in 0.02 M glycerol + 1 M KOH within the potential window of -1.0 - 0.5 V@1V/s for 100 cycles. This was followed by GEOR performance evaluation through CV measurements in the same solution as above, for 40 cycles at 0.1 V/s.GEOR was also evaluated using LSV, performed in the potential window of −1.0 − 0.4 V@0.005 V/s. CVs in blank (1.0 M KOH) were also collected by cycling within the same potential window as mentioned above at 0.1 V/s for 3 cycles as background response. All electrochemical measurements are reported without *iR* compensation as electrode size, and thereby, the current scale is small enough to neglect the effect of *iR*-drop.

Product Quantification via Flow Electrolysis. We employed a lab-made flow electrolyzer to study product speciation under continuous flow conditions.[16,40] A constant flow rate of 2 mL/min of electrolyte was maintained over both the WE (0.1 M Glycerol + 1.0 M KOH) and CE (1.0 M KOH) channels using a peristaltic pump (Cole Parmer Masterflex L/S). The two electrode channels were separated using an anion exchange membrane (AEM, Fumasep FAA-3-PK-75), conditioned by soaking in 1.0 M KOH for 24 h. A Ni foil coated with Pt (t = 8.0 min sputter) was employed as the CE. Three different WEs−one planar and two electrodeposited ones were used, where a Ni foil (conducting substrate) was coated with Au (t = 5.0 min sputter), Au (E_l = −0.6 V, PW = 0.2 s), and Au (E_l = −1.4 V, PW = 1.0 s). Using a T-junction, an Ag/AgCl RE was connected to the glycerol electrolyte stream running through the WE channel. All results for flow experiments are plotted versus RHE, where the potentials were converted using the formula

$$E_{RHE} = E_{Ag/AgCl} + E^0_{Ag/AgCl} + (0.0591 \times pH)$$

The electrochemical experiments were performed at constant anode potentials using a CHI 760e potentiostat. Like IAE-based experiments, the electrodes were first conditioned by cycling for 100 cycles at 1.0 V/s between −0.1 − 1.6 V (vs RHE) and then cycling within the same potential window at 0.1 V/s for 10 cycles. We then performed chronoamperogram (CA) measurements at fixed potentials for 240.0 s, and products were sampled during the last 120.0 s and analyzed using high-performance liquid chromatography (HPLC). The charge passed during this sampling period was measured for Faradaic efficiency (FE) calculations, and the current density was averaged for J−V plots. The liquid products were analyzed using a Nexera 40 Series HPLC (Shimadzu Scientific Instruments) equipped with a Bio-Rad Aminex HPX-87C column. The liquid samples were neutralized with 0.5 M H_2SO_4 in a 1:1 v/v ratio to maintain a pH of 1−3. A column temperature and flow rate of 60 °C and 0.6 mL/min were maintained, and a 20 μL of liquid sample (0.05 M H_2SO_4 mobile phase) was injected into the column. The products were detected using a ultraviolet−visible (UV−vis) detector with a λ = 210 nm. Since only the anode products were being investigated, and as glycerol majorly forms liquid products, the gaseous products were not analyzed. The concentration (mM), Faradaic efficiency (%), and relative selectivity (%) for each major product were calculated using the equations

$$\text{conc.}_{prod} = \frac{\text{intensity}}{\text{slope}_{prod}}$$

$$FE_{prod}(\%) = \frac{\nu \times t \times \text{conc.}_{prod}}{Q/(z_{prod} \times F)} \times 100$$

where the slopes for each product were determined by individual calibration curves, ν = flow rate (mL/min), t = duration of electrolysis (s), Q = charge passed during each electrolysis CA, F = Faraday's constant (96,485 C/mol), z = number of electrons transferred to form one mole of the product. Z_{oxalic}, $z_{glyceric}$, $z_{glycolic}$, z_{formic}, and z_{acetic} were 22:3, 4, 10:3, 8:3, and 8:3 respectively.

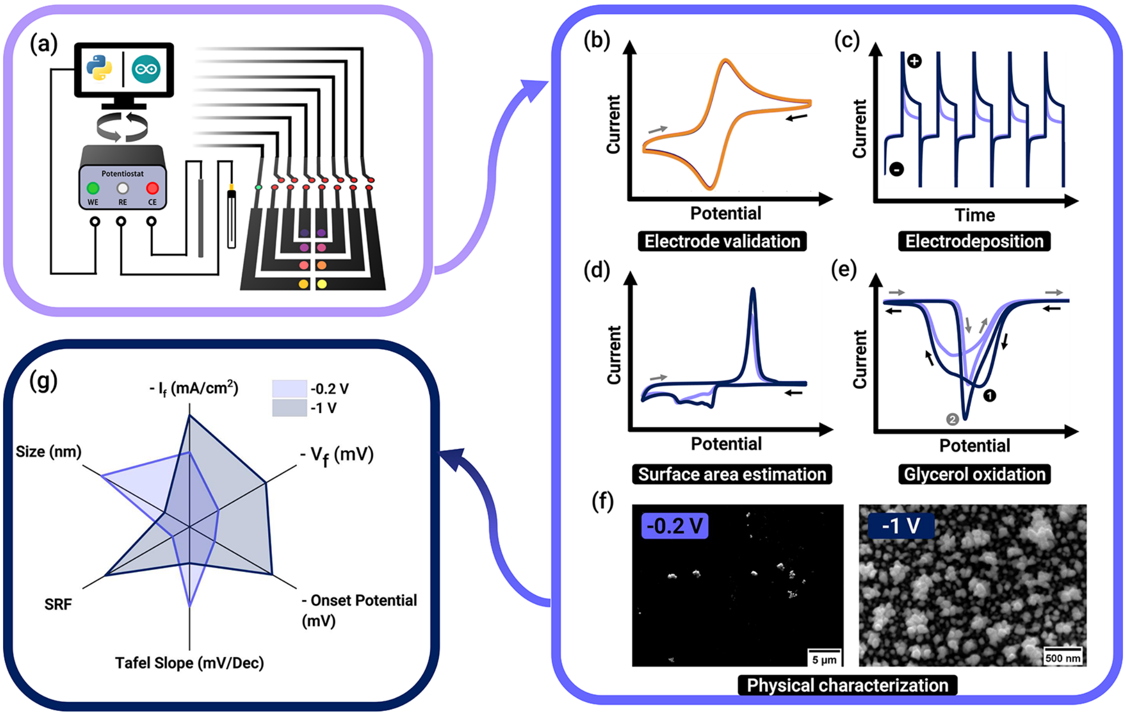

Figure 1. Schematic of electrocatalyst screening workflow. (a) Animated representation of automated electrochemical setup using an 8-electrode IAE array device powered by HardPotato. (b) Cyclic voltammetry on IAE array device for electrode size validation using electrochemical oxidation of ferrocenemethanol (1.16 mM FcMeOH + 0.1 M KNO_3) at scan-rate = 0.5 V/s. Black and gray arrows indicate forward (anodic) and reverse (cathodic) potentials sweeps. (c) Chronoamperogram representing the electrodeposition of Au at two different reduction potentials: −0.2 V (purple) and −1.0 V (blue). (d) Cyclic voltammogram in 0.5 M H_2SO_4. (e) Cyclic voltammogram in 0.02 M Glycerol +1.0 M KOH. (f) SEM images of Au deposited at −0.2 and −1.0 V, respectively. (g) Spider graph comparing figures of merits for comprehensive evaluation of catalytic performance.

Physical Characterization. Morphology and particle size analysis of Au NPs was performed using the FEI Quanta FEG 450 environmental scanning electron microscopy (ESEM). Operating conditions during image acquisition were pressure = 0.98−1.00 Torr; dwell time = 10 μs, accelerating voltage = 20 kV, current = 5 mA, magnification = 10k−60 kx. Crystal structure information on Au NPs was obtained by collecting X-ray Diffractograms on the Rigaku MiniFlex 600 instrument with a Cu Kα (λ = 1.5418 Å) X-ray source operated under 40 kV, 15 mA, and a 1.2°/min scan-speed. Denton Vacuum Desk V sputter coater was used to sputter-coat IAE devices and Ni foils using default Cr and Pt targets.

■ SCREENING METHODOLOGY

Figure 1 depicts the experimental workflow in this manuscript, consisting of (a) device integration, (b−f) semiautomated electrodeposition and characterization, and (g) data analysis. Toward device integration, we first followed a microfabrication protocol[41] where we fabricated an array of individually addressable electrode (IAE) devices, each containing eight Au electrodes (r = 100 μm) on which distinct electrochemical protocols could be programmed. A concise overview of the fabrication steps, along with a workflow schematic, can be found in the Materials and Methods Section and Figure S1. We established electrical connections to these devices using a flexible ribbon cable incorporating anisotropically conducting tape between the cable and the device. These array chips were then used in conjunction with an open-source Python API − HardPotato, enabling precise control over each electrode in the array. This control was achieved using an 8-to-1 multiplexer powered by an Arduino Uno, facilitating automated electrochemical operations at each of our electrodes via a printed circuit board adaptor depicted in Figures 1a and S2, which allowed us to switch from electrode #1 to #8 serially. This setup ensured effective cross-communication between the PC, potentiostat, multiplexer, and IAE device, leveraging the integration of the HardPotato API with the IAE array.

Prior to any electrocatalytic measurements, we benchmarked our bare electrodes using a reliable, fast redox mediator (ferrocenemethanol) at all the electrodes on our array (Figure 1b). To accurately determine the real electrode radius and identify any outliers resulting from the microfabrication process, we performed Randles—Ševčik analysis using cyclic voltammetry at various scan rates. Following this step and after thorough rinsing, we electrodeposited Au catalysts using chronoamperometry by pulsing between the open-circuit potential (OCP) and a reducing potential. We systematically varied (i) the pulse width (PW) and (ii) the reduction potential (E_l) to deposit an array of Au catalysts, each exhibiting distinct physical and electrochemical properties. A representative electrodeposition chronoamperogram is illustrated in Figure 1c, where E_l is modulated between −0.2 and −1.0 V while maintaining a constant PW of 60.0 s. Post Edep, to electrochemically characterize the Au catalyst deposited, we performed cyclic voltammetry in 0.5 M H_2SO_4 (Figure 1d). This analysis provided insights into the electrochemical surface area (ECSA) and the surface roughness factor (SRF), defined as the ratio of ECSA to the geometric area of the electrode.

Finally, rigorous electrocatalytic characterization of these Au catalysts was performed in 0.02 M Glycerol +1.0 M KOH.

https://doi.org/10.1021/acscatal.4c04190
ACS Catal. 2025, 15, 639−652

Figure 1e depicts a typical GEOR CV response on an Au catalyst. Later sections provide a more in-depth analysis of the GEOR performance. There have been several excellent reports discussing the shape of voltammograms and mechanisms for the electro-oxidation of alcohols on gold electrodes in alkali media.[42−46] Briefly, glycerol is oxidized during the forward (anodic) sweep and this process is constrained by electrode kinetics and the availability of active sites. As the potential is made more positive, gold oxide (AuO_x) and other reaction intermediates accumulate, diminishing the activity and thus resulting in a peak labeled as Peak 1 (Figure 1e). On the reverse (cathodic) sweep, the potential reaches a level sufficient to reduce the gold oxide layer, refreshing the metallic sites, thus leading to another set of oxidation peaks (Peak 2) associated with the oxidation of adsorbed GEOR intermediates or nearby glycerol molecules. In addition to CVs, we also performed linear sweep voltammetry (LSV) measurements to obtain onset potentials and Tafel slopes, which are critical metrics in electrocatalysis studies.

We further leveraged our IAE array design beyond electrochemical characterization, enabling morphological characterization via scanning electron microscopy (SEM). This approach directly correlates the catalysts' electrochemical performance with their physical properties. Illustrated in Figure 1f are SEM images of gold (Au) electrodeposits synthesized at $E_1 = -0.2$, and -1.0 V. This capability to adjust particle size exemplifies the versatility of our method, supporting rapid and efficient synthesis and evaluation of micro/nanoscale electrocatalysts directly on a single device.

As an illustration (Figure 1g) of how all aspects in our methodology come together, when we contrasted the GEOR performance of Au deposited at −0.2, and −1.0 V, we noted an enhancement in current density, a decrease in peak positions, a lower onset potential, and a reduced Tafel slope, all of which are markers for improvements in electrocatalytic performance. The Edep characterization and comparison were performed for all 28 unique conditions tested, including 2 additional repeats per condition, thus demonstrating the reliability and versatility of our methodology.

■ RESULTS AND DISCUSSION

Electrode Validation with FcMeOH. We first depict how the IAE devices provide a reproducible platform on which the geometric area and electrochemical responses of each bare electrode are comparable. Leveraging HardPotato's capabilities, we performed CVs of the one-electron redox mediator ferrocenemethanol (FcMeOH) sequentially on each electrode of the IAE array device (Figure 2a). CVs were performed by scanning between −0.2 and 0.5 V and back at varying scan rates ranging from 0.1, to 1.0 V/s at each electrode (Figures 2b and S3). From Figure 2b, it is evident that the oxidation of FcMeOH undergoes an electrochemically reversible reaction from which analysis of the voltammetric features can help confirm the geometric area, and thus the radius, of each electrode. We conducted Randles−Ševčík (RS) by plotting the anodic peak current (I_{pa}) as a function of the square root of scan rate and applied linear regression to estimate the slope, from which the accurate radius of the electrode was derived. Prior to the measurements, we determined the concentration and diffusion coefficient of the FcMeOH solution to be 1.16 mM and 7.25×10^{-10} m^2/s, respectively, through steady-state measurements at an ultramicroelectrode (UME) (Figure S4).

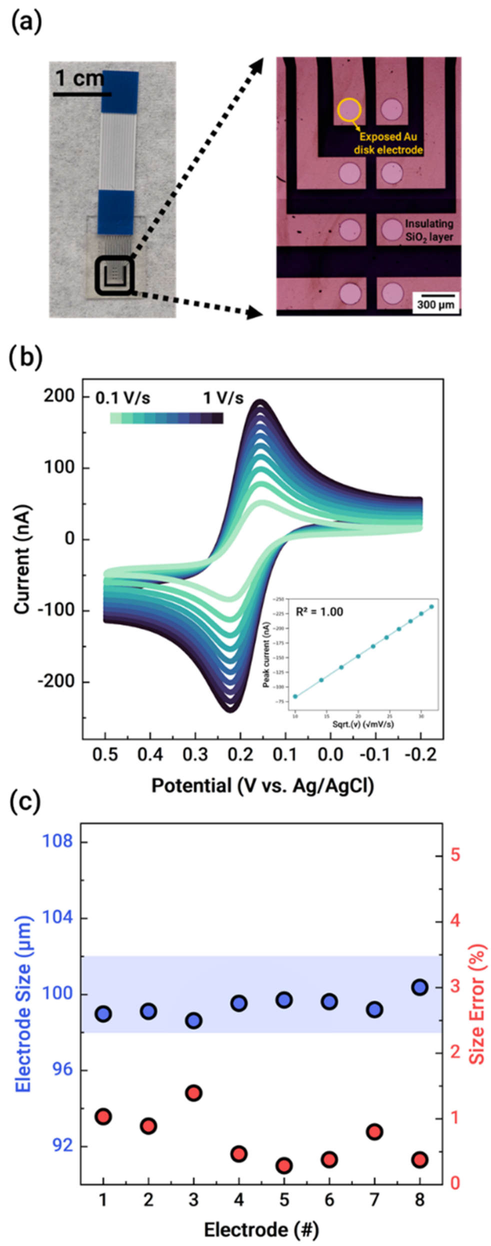

Figure 2. Electrode benchmarking using FcMeOH. (a) Picture of an IAE array device (left) and an optical micrograph (right) of all the 8 Au disk electrodes ($r = 100$ μm) available on each IAE array device. (b) CVs for FcMeOH oxidation at each electrode on the IAE array at varying scan rates (0.1, 0.2, 0.3, 0.4, 0.5, 0.6, 0.7, 0.8, 0.9, 1.0 V/s). Inset (bottom-right): Scatter plot of anodic peak currents vs scan rate$^{1/2}$ with the linear fit. Experimental conditions: 1.16 mM FcMeOH + 0.1 M KNO_3. WE: Au; CE: Graphite rod; RE: Ag/AgCl. (c) Scatter plots of the real electrode radius (left axis) and the corresponding size error (right axis) obtained from the slope of the current vs scan rate$^{1/2}$ plots.

Primarily, RS analysis enables us to confirm the nature of mass transport occurring at the surface of these electrodes, which is linear diffusion (Figure S5), evidenced by excellent conformity with an $R^2 \sim 1$ at all the electrodes on the array device. Additionally, we utilized RS analysis to quantify the yield of the microfabrication process. Figure 2c illustrates the calculated radius of each electrode and the corresponding error in size relative to the nominal 100 μm (radius) electrode. All eight electrodes on our device have identical feature sizes with

https://doi.org/10.1021/acscatal.4c04190
ACS Catal. 2025, 15, 639−652

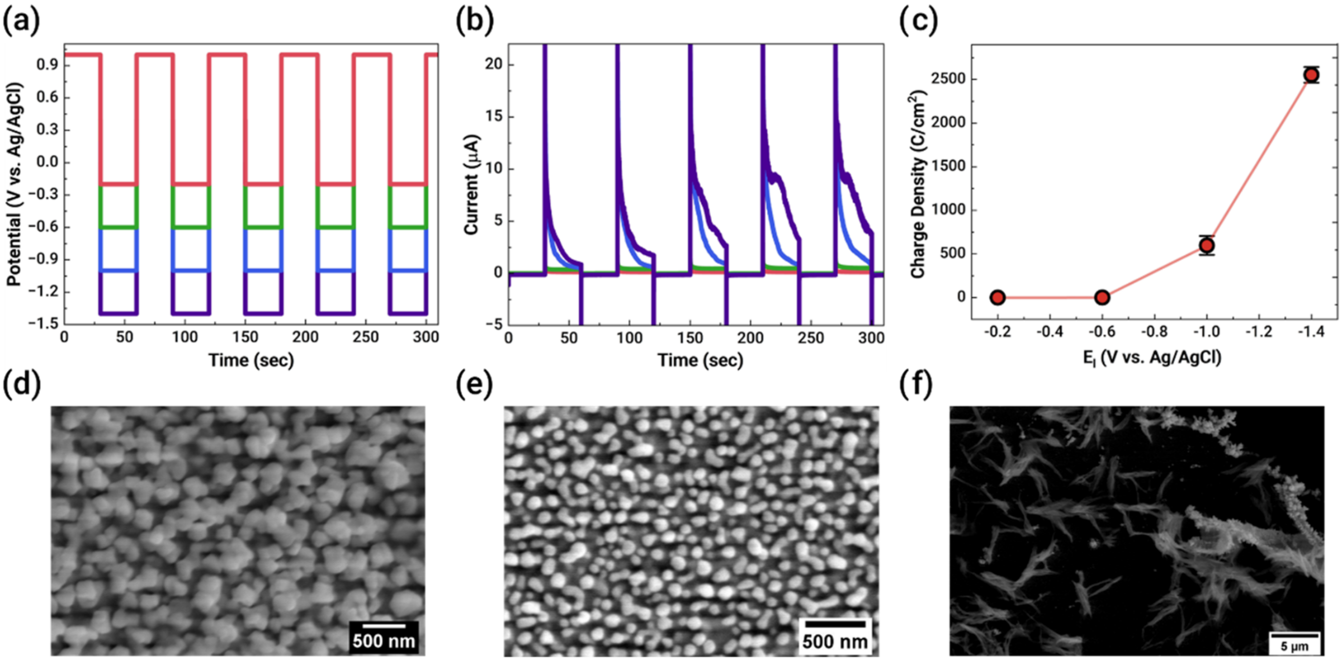

Figure 3. Representative plots for pulsed electrodeposition of Au NPs. (a) Potential-time waveform employed during electrodeposition. The potential was switched from E_h = 1.0 V (const.) to varying E_l values after the = 30.0 s (total = 600.0 s, i.e., n_{seg} = 20). E_l = −0.2 V (red), −0.6 V (green), −1.0 V (blue), −1.4 (purple). (b) Corresponding current−time plot generated during the application of potential waveform. (c) The total charge passed during each Edep experiment as a function of E_l Experimental Conditions: 1.0 mM $HAuCl_4$ + 0.5 M H_2SO_4. WE: Au (sputter), CE: Graphite rod, RE: Ag/AgCl. (d−f) SEM Images of Au particles deposited at −1.4 V (PW = 0.05 s), −0.6 V (PW = 0.05 s), and −0.6 V (PW = 5.0 s), respectively.

deviations of ±1.3 μm, corresponding to a size error <1.5%. We attribute this small % error in size to the swelling or erosion of insulating photoresist walls during the microfabrication stage. This analysis also highlights a key advantage of our electrochemical setup: the ability to perform reliable measurements at nA-scale using disk electrodes, with minimal limitations from heterogeneities in electrical conductivity, potential drifts due to the use of quasi-reference electrodes, and ohmic losses arising due to larger currents at larger electrodes, most which are some common limitations of HT Echem screening technologies.

While our microfabrication process does not achieve a 100% success rate, the FcMeOH measurements allow the identification of faulty electrodes. A distribution of % error in electrode radii of all electrodes used in this study is depicted in Figure S6, and any electrode with a size deviation of >10% was excluded from future measurements. Such deviations are expected to occur during the microfabrication stages due to factors such as electrode shorting, human errors, scratches on the micropatterns, or high resistivity in the electrical connections resulting from nonuniform etching of silicon oxide layers. The CV plots of faulty electrodes are shown in Figure S7, where these errors are apparent in the form of purely resistive CVs exhibiting ohmic and/or capacitive behavior or significantly higher slopes during RS analysis compared to the ones in Figure 2.

Pulsed Electrodeposition of Au NPs. In this section, we showcase our screening methodology's application toward probing the influence of driving force and time scales on the Edep rates and, consequently, the morphology of Au deposits. We employed pulsed electrodeposition (PED), a chronoamperometric technique that alternates short pulses between a higher potential (E_h) and lower potentials (E_l) across multiple segments.[38,47,48] We controlled the driving force and time scales by manipulating the deposition potential and pulse width (PW), respectively. Figure 3a illustrates the Au Edep potential waveform, pulsing between E_h = 1.0 V and E_l = −0.2, −0.6, −1.0, and −1.4 V for 30.0 s at each potential, repeated across 20 segments (n_{seg}), with the corresponding chronoamperogram (CA) depicted in Figure 3b. For simplicity, we maintained the higher-end potential constant in our experiments, fixing it at E_h = 1.0 V, which closely approximates the cell's open-circuit potential, facilitating the replenishment of Au precursor after each reduction segment. Holding the total electrodeposition time constant (t_{Edep} = 5.0 min), we systematically varied the PW from 60.0 to 30.0, 5.0, 1.0, 0.2, 0.05, and 0.01 s, respectively, at each E_l. With each combination of unique deposition parameters—a total of 28 conditions—and each condition done in triplicate on different days and random devices to track the reproducibility of each result, we conducted 84 full experiments overall.

The CAs in Figure 3b represent a typical Edep process characterized first by an initial exponential current decay due to double-layer capacitance (DLC), followed by a gradual rise due to continuous nucleation of fresh Au site, and finally trailed by a Cottrell decay. The effect of E_l (driving force) on the rate of electrodeposition is evident in Figure 3c, where we measure the total reductive charge (Q_{red}) passed in each CA. Q_{red} increases exponentially from 0.4 to 2553 C/mm^2 when the t_{Edep} and PW are held constant at 5.0 min and 0.05 s, respectively, and E_l changes from −0.2, to −1.4 V. Comparative SEM analysis of electrodeposits at different E_l (Figure 3d,3e) reveals a significant increase in particle nucleation density at the more negative potential attributed to a substantially larger driving force applied during deposition. In addition to changes in particle density, a considerable

https://doi.org/10.1021/acscatal.4c04190
ACS Catal. 2025, 15, 639−652

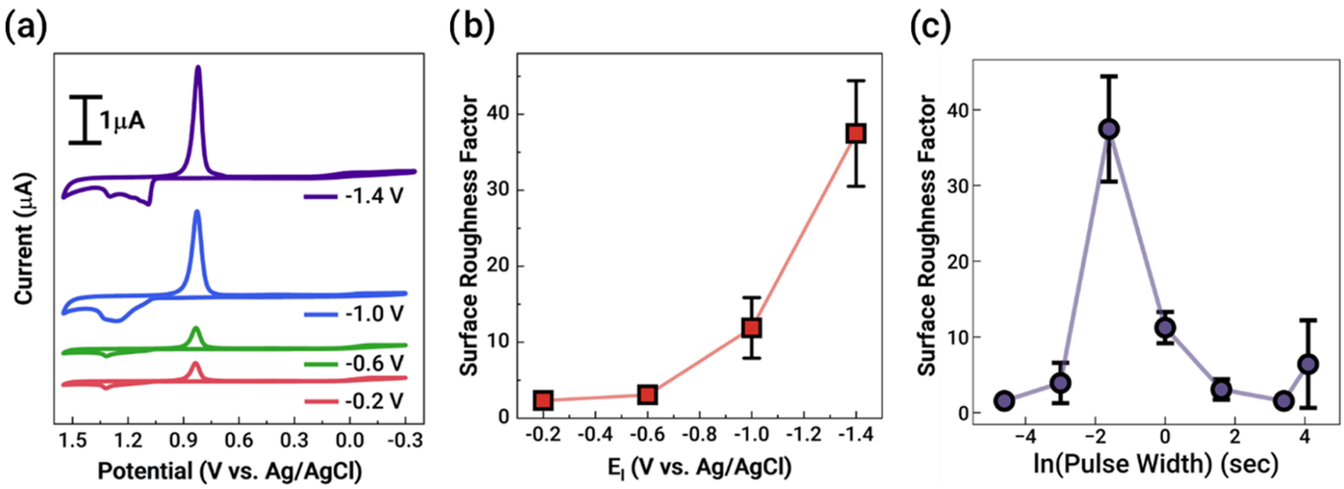

Figure 4. Electrochemical surface area estimation of selected results from CV in 0.5 M H_2SO_4. (a) Representative CVs performed at Au deposited at varying E_l, holding PW fixed at 0.2 s depicting distinct features present at different Edep conditions (b, c) Surface Roughness Factor plotted as a function of E_l (fixed PW = 0.2 s), and PW (fixed E_l = −1.4 V) respectively.

increase in particle size from 117 ± 21.2, to 280 ± 66.5 nm (Figure S8) was observed, and the morphology also shifts from a predominantly spherical shape to a cuboidal/tetragonal nanoparticle (NP), with higher agglomeration.

Unlike Figure 3c, the variation of Q_{red} with PW is more complicated, as the electrodeposition trends vary based on applied reduction potential (Figure S9). At the more negative E_l, a peak-shaped plot emerged with a maximum at ∼ PW = 0.2 s. The influence of PW on Au morphology can be understood by analyzing the SEM images of the deposits. As illustrated in Figure 3e,3f, the morphology transitions from spherical NPs (117 ± 21.2 nm) with uniform coverage to large needle-shaped microclusters (4.43 ± 2.31 μm) with poor electrode coverage when the PW changes from 0.05 to 5.0 s. Shorter PW favors nucleation over particle growth, resulting in high particle density and smaller sizes. Conversely, longer deposition times lead to more pronounced particle growth and coalescence due to extended durations of applied driving force, resulting in a noticeable increase in particle size.[49] Moreover, the decreasing particle density with increasing diameter is likely due to electrochemically enhanced Ostwald ripening, as reported by Redmond et al., occurring during the experimental time scale, resulting in these larger Au particles.[50] These results underscore how the interplay of a vast space of electrodeposition variables and factors condition the formation of significantly different structures, which, as we will show in the following section, have distinct electrochemical properties. Our approach swiftly enables the semiautomated deposition and analysis of these structures, including repeats, to ensure reproducibility.

Electrochemical Characterization. We determined the electrochemical surface area (ECSA) and the surface roughness factor (SRF) of the gold (Au) electrodeposits through AuO_x stripping analysis performed in 0.5 M H_2SO_4, a well-established technique for estimating ECSA.[51] We performed CVs by sweeping the potential between −0.35 V and 1.55@0.1 V/s (Figures 4a and S10). A series of peaks were observed on the anodic sweep from 0.95 to 1.45 V, corresponding to the oxidation of surface gold sites, with each peak typically associated with specific Au surface orientations. Conversely, we observed a sharp Gaussian-shaped peak at approximately 0.86 V on the cathodic sweep, corresponding to the reduction of surface AuO_x. This peak was the basis for calculating the ECSA (Figure S11) and, subsequently, the SRF. To facilitate the analysis of large data sets, we employed a custom-written Python script for batch processing of all CVs. This involved automatic plotting, baseline fitting of the reduction peak, and estimation of Q_{AuOx} − the charge passed stripping of oxide peak (shaded region under peak @0.86 V in Figure S10). The scripts also enabled the subsequent plotting of SRF (obtained from Q_{AuOx}) as a function of the Edep parameters, as depicted in Figures 4b,4c, and S12. Note that these CVs were performed for over 5 cycles on each electrode as repeated cycling is known to induce surface restructuring and electrochemically roughen the electrode (refer to Figure S13).[52]

As demonstrated in the previous section and corroborated by existing literature, increasing deposition potentials lead to the formation of higher-density nanoparticles (NPs) with rougher surfaces. According to the Butler−Volmer kinetic model, the nucleation rate is expected to increase exponentially with an increase in potential.[39] Baker and co-workers have illustrated that controlling the E_l can effectively manipulate the kinetics of metal ion reduction and, consequently, the nucleation rate.[53] They report a lower particle yield at less negative E_l values, resulting in more spherical nanostructures that evolve into cubic nanoparticles with sharper edges and significantly higher particle yields at more negative E_l values. A similar effect manifests in our study as well, albeit the structural changes are not as evident due to the absence of chemical additives. However, the effects on particle yield are striking, as confirmed by SEM images (Figure 3c,3d) and ECSA measurements. Specifically, there is a significant increase in the surface roughness factor (SRF) from 2.3 to 37.5 as the E_l changes from −0.2, to −1.4 V (vs Ag/AgCl), as illustrated in Figure 4b.

An interesting relationship emerges when correlating ECSA with the PW during electrodeposition. Holding other variables constant (t_{Edep}, E_l, and E_h), we study the ECSA-PW trend as shown in Figure 4c. We hypothesize that the Edep process is constrained by the dominance of DL discharge at very short pulses. To maintain the same t_{Edep}, the number of segments (n_{seg}) varied with PW—for example, at PW = 0.05 s, n_{seg} is 12,000, compared to just 10 segments at PW = 60.0 s. Thus, at very short PW (0.01 and 0.05 s), DL discharge primarily

https://doi.org/10.1021/acscatal.4c04190
ACS Catal. 2025, 15, 639−652

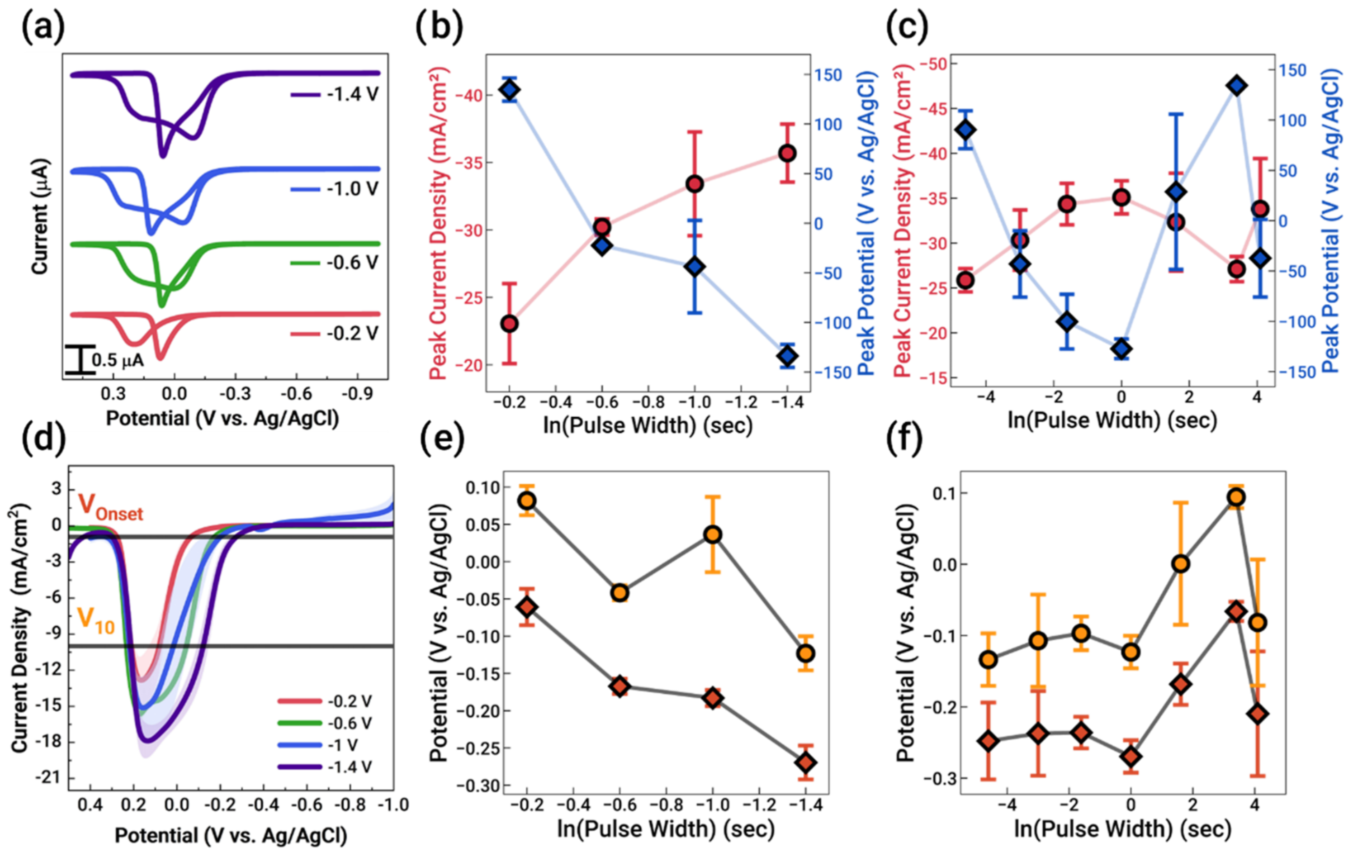

Figure 5. Evaluating GEOR performance as a function of Au Edep parameters. (a) Representative GEOR CVs at different E_l and fixed PW (1.0 s). (b, c) Peak current density (I_f) and peak position (V_f) during the forward sweep of the CV are presented as a function of E_l when PW = 1.0 s and as a function of PW when E_l = −1.4 V, respectively. (d) Representative GEOR slow-scan LSV at different E_l when PW = 1.0 s. (e, f) GEOR characterization by Onset Potential (orange) and V_{10} (yellow) as a function of E_l and PW, respectively.

contributes to the currents measured in each reduction segment as opposed to the Edep process. This hypothesis is supported by a lower SRF of 1.54 recorded at a PW of 0.01 s (close to a typical 1.0−1.2 for a planar electrode) compared to 37.5 when PW reaches 0.2 s. However, the SRF declines to 11.2 as PW extends to 1.0 s and further decreases to 6.4 at 60.0 s. This trend of variation in PW remains consistent across different electrodeposition potentials, as seen in Figure S12. This significant decline at longer PWs can be attributed to drastic morphological changes (dendritic growth, Figure 3d), leading to the formation of microstructures and, consequently, a reduced electroactive surface area.

However, our triplicate measurements reveal noticeable discrepancies in the ECSAs measured for gold deposited under varying conditions. As illustrated in Figure S14, the inconsistency in Au loading is influenced by both the E_l as well as the PW. Notably, when E_l is set to −0.6, −1.0, and −1.4 V, there is a visible deviation in measured ECSA at short PWs (0.05 and 0.20 s). We speculate that this may be due to larger hydrogen evolution reaction (HER) rates occurring at these potentials. The generation of hydrogen bubbles during HER likely obstructs the electrode surface, leading to irregularities in gold deposits.[54] This variance in ECSA occurs despite no significant deviation in the charge passed during the reduction segments (Figure S9). This suggests that the Coulombic efficiency split between HER and metal ion reduction is inconsistent at these shorter PWs. The ability to capture reactive trends and determine the electrodeposits' robustness is a feature conveniently enabled by our semiautomated approach.

Glycerol Electro-Oxidation Reaction. The electrochemical study of glycerol oxidation was primarily carried out by performing CVs within the range of −1.0 −0.5 V (V vs Ag/AgCl) in 0.02 M glycerol +1.0 M KOH at 0.1 V/s (Figure 5a). We performed our experiments in alkaline conditions owing to the higher reactivity of glycerol in these conditions, as pH can influence current density and product distribution.[6,55,56] The fast kinetics in alkali media are attributed to the base-catalyzed glycerol deprotonation step leading to the generation of glyceroxide species, whose adsorption on the active site is the rate-determining step in the oxidation reaction.[46] Similarly, other reports discuss the influence of increasing glycerol concentration on the electrochemical performance. Furthermore, while the peak current densities have been reported to rise due to an increase in reactive species in solution, the peak positions and the onset potentials shift toward more positive potentials explained by the Langmuir−Hinshelwood-like mechanism due to competition adsorption between glycerol and OH^-.[56] We found that a concentration of 0.02 M glycerol afforded an easily measurable response while preventing the blocking of Au sites toward OH^- adsorption.

Prior to GOR measurements, CV at 1.0 V/s was performed in the same electrolyte as a conditioning step to allow for surface reconstruction and stabilization of active sites (Figure S15).[57] A comprehensive compilation of all GEOR CVs performed in this study is shown in Figure S16, with each color palette representing each E_l employed during deposition and

https://doi.org/10.1021/acscatal.4c04190
ACS Catal. 2025, 15, 639−652

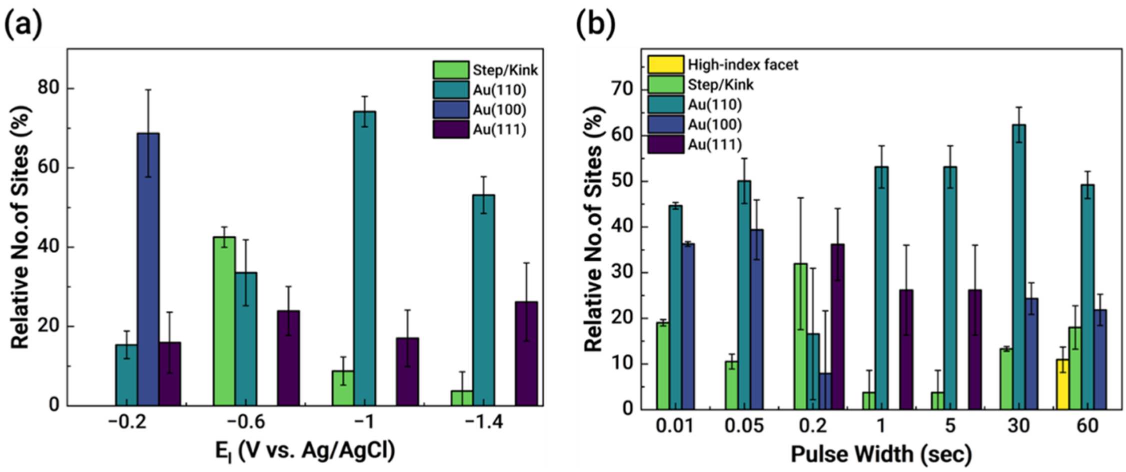

Figure 6. Relative no. of reactive Au sites as a function of (a) E_l and (b) PW. Surface facets were identified based on peak assignments from literature.[59−61] Note: Sputtered Au recorded to have exclusively Au(111) sites, with a relative no. of sites (~100%).

each independent CV within the column representing the GEOR CV of the Au catalyst deposited at a different PW. To thoroughly test the robustness of our approach, the error associated with each measurement is shown as a shaded region representing the standard deviation around the mean, from n = 3 different catalyst deposits. As illustrated in Figure 5b,5c, the electrocatalytic performance can be evaluated using several CV features, but we focused on the peak current density (I_f) on the anodic forward sweep and its corresponding position (V_f).

One common oversight in GEOR literature is the lack of discourse on the GEOR CVs over multiple cycles, as most catalysts see activity decay upon cycling due to surface passivation, reconstruction, or metal dissolution. Addressing this oversight, we performed our GEOR CVs for over 20 cycles and have reported the CV features of the last cycle in Figure 5b,5c. We also report the I_f and V_f values for the first and the 10th cycles of CVs in Figure S17 to visualize trends in activity as a function of cycling. Additionally, we also performed linear sweep voltammogram (LSV) measurements (Figure 5d) at a scan rate of 0.005 V/s to measure the onset potential, defined as the potential needed to achieve 1.0 mA/cm^2, as well as the potential needed to achieve a current density of 10.0 mA/cm^2, which are denoted by V_{Onset} and V_{10} respectively. Figures 5e,5f, and S18 depict the V_{Onset}, and V_{10} plotted as a function of PW and E_l, while the corresponding LSVs from which this data was obtained can be found in Figure S19. Furthermore, we generated Tafel plots to determine Tafel slopes from these LSVs using basic data processing scripts, as shown in Figure S20.

We first validated our technique by exploring the dependence of GEOR on the deposition potential, as dependencies on this parameter are well established in the literature for alcohol electro-oxidation.[38,48,58] Figure 5a depicts GEOR CVs of Au deposited at varying E_l values, maintaining PW at 1.0 s. Studying the peak features of this CV as a function of E_l reveals a direct correlation between deposition potential and GEOR activity (Figure 5b). We observed a direct correlation between deposition potential and GEOR activity, with a 52% increase in I_f and a 0.250 V reduction in V_f as E_l changes to a more negative potential. This improvement in catalytic activity is further corroborated by the measured trends in V_{Onset} and V_{10}, as −0.208 and −0.205 V shifts were recorded, respectively. While we did not rely on the Tafel slope as a critical tool for measuring catalytic activity, basic Tafel analysis (Figure S20e–h) further reinforces our findings by indicating a 13 mV/Dec reduction in the Tafel slope.

While the dependence of GEOR activity on E_l on Au has been previously reported, our approach allowed us to swiftly explore the impact of PW, as well. Across all four E_l potentials examined; we identified an optimal GEOR activity at around PW = 1.0 s. This optimized PW duration minimized DLC effects and was sufficiently brief to induce preferential nucleation of NPs with highly active sites while preventing particle agglomeration at much longer PWs (>1.0 s). While observing PW−GEOR performance trends in the case of E_l = −1.4 V, as depicted in Figure 5c, we noticed a 36% increase in I_f and a 0.22 V reduction in V_f as PW varied from 0.01 to 1.0 s. Unlike reactive trends with E_l, the V_{onset} and V_{10} changes are less drastic with PW variation within this range (Figure 5f).

As E_l is made more negative, there is an increase in mass loading of Au on the electrocatalyst, and this parameter is correlated to a higher activity, as grasped from Figure 5b,5e. However, CV analyses in 0.5 M H_2SO_4 allow us to infer surface properties that are likely more relevant to electrocatalysis, such as the faceting of Au deposited under varying conditions. Kim et al. reported that the presence of Au(110) sites significantly enhances electro-oxidation activity.[59] Similarly, there have been other reports that explore the facet-dependent activity of Au(100), Au(111), and Au(110) for alcohol oxidation, underscoring the importance of these facets in reducing the energy barrier for $Au(OH)_x$ formation.[60,62,63] Figures 6 and S21 illustrate how CV data can be analyzed to estimate the presence of specific Au facets at various electrodeposition conditions. Although this analysis only estimates the type of surface site, it is quite revealing to observe great diversity in the voltammetric profiles of this $Au(OH)_x$ formation region. A common trend observed in cases of varying E_l (Figure 6a) and PW (Figure 6b) is the correlation between step/kink edges and Au(100) sites with GEOR activity, where a lower relative number of these sites results in enhanced activity. Conversely, the presence of Au(111) + Au(110) sites results in higher activity. One important test for this analysis is to provide insight into stark differences in reactivity. For example, a sharp peak at around 1.0 V in the case of E_l = −1.4 V and PW = 60.0 s could likely correspond to a higher index faceted site such as Au(210) or Au(310) formed upon extensive electroreduction.

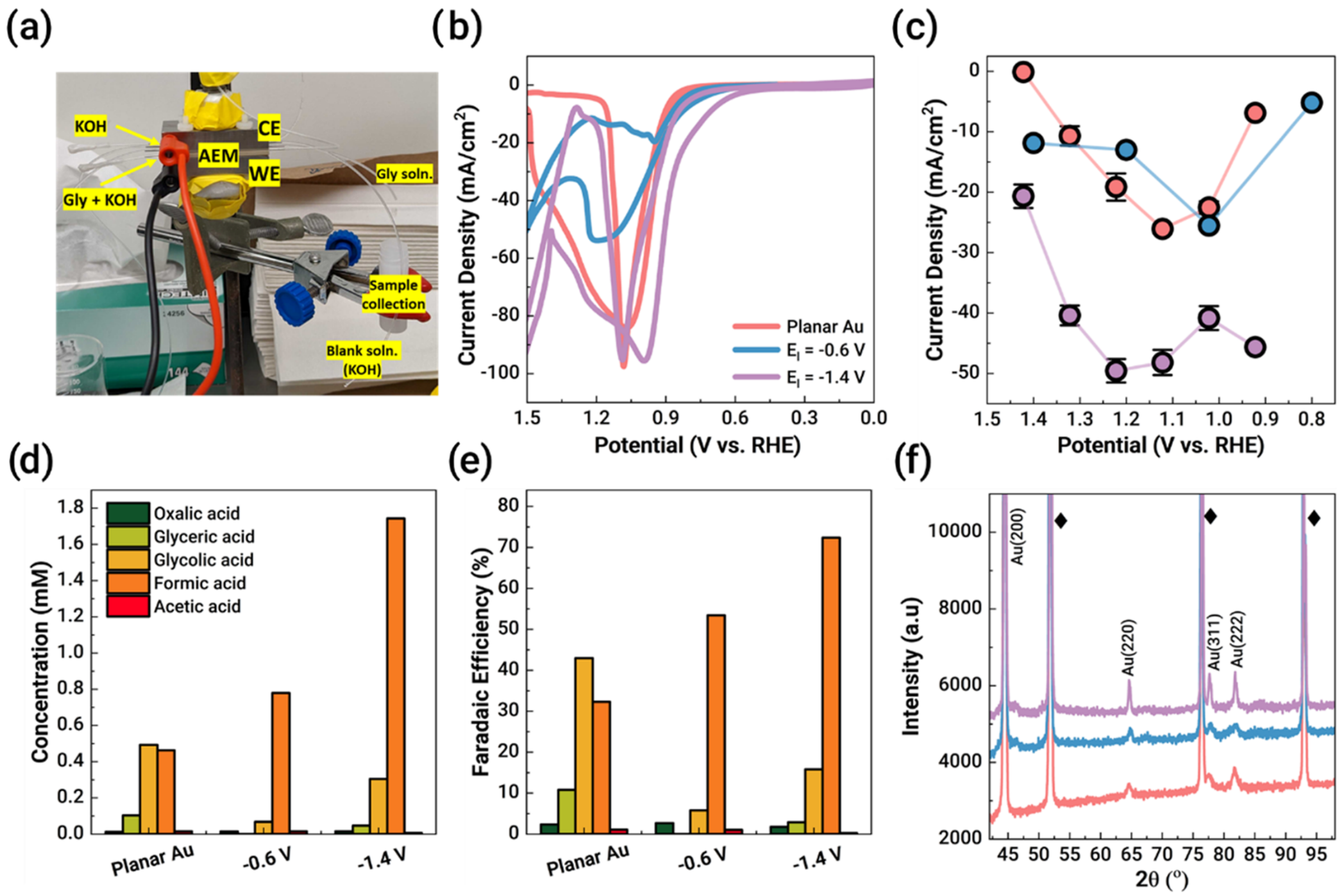

Figure 7. Glycerol electro-oxidation via flow-electrolysis. (a) Picture of lab-made flow-electrolyzer cell. (b) GEOR CV performed at 0.1 V/s. The 20th cycle is represented in the plot. (c) $J-V$ curves representing mean current density obtained from running a 240.0 s CA. (d) Concentration and (e) Faradaic Efficiencies of all major products quantified via HPLC when E = 1.4 V vs RHE. (f) X-ray Diffractograms of Planar Au (peach), Au(E_l = −0.6 V) (blue), and Au (E_l = −1.4 V) (violet). Note: Peaks labeled with ♦ correspond to the underlying Ni foil.

It is precisely this catalyst that showed a sudden increase in catalytic performance as PW increased from 30.0 to 60.0 s in Figure 5c. Interestingly, such comparisons hold even for underperforming catalysts produced at greatly different PW. Consider the surface and activity comparison of catalysts obtained at E_l = −1.4 V and PW 0.01 and 30.0 s. These two catalysts display a nearly identical surface feature distribution (Figures S21a,f, and 6b) as per our analysis, and they also exhibit the same lowest catalytic GEOR activity evident from Figure 5c.

Scale-Up Flow Electrolyzer Testing. Finally, this section addresses the translations of our observations from the semiautomated electrocatalyst screening to a flow reactor. A critical challenge most electrocatalyst screening architectures face is their scalability to large-scale, real-world electrolyzer systems. To address this, we validated the results obtained from our screening methodology by scaling up synthesis from μm-scale electrodes to electrodes of 3 cm^2 using a custom-made cell holder, as shown in Figure S22. This allowed for the electrodeposition of Au nanoparticles (NPs) on a Ni foil. Reports have indicated that employing flow-electrolyzers to study product speciation and Faradaic efficiencies (FE) is an effective strategy for evaluating the practical electrochemical performance of catalysts.[12,40,64,65] To this end, we used a lab-made flow electrolyzer (Figure 7a) cell to study the performance of GEOR of the top-performing candidates from IAE screening experiments.[16]

Collating the entire range of GEOR performance metrics across all E_l and PWs provides valuable insights into activity, reproducibility, and stability. While Au(E_l = −1.0 V, PW = 0.2 s) did yield an initial I_f > −40.0 mA/cm^2 during the first cycle (Figure S17g,i), The I_f and V_f fluctuated greatly across the 20 cycles, indicating poor catalyst stability. Additionally, this Edep condition also displayed poor consistency during ECSA measurements (Figure S14), suggesting poor reproducibility of this condition. In contrast, two other top candidates demonstrated strong activity, reproducibility, and stability: Au(E_l = −0.6 V, PW = 0.2 s) and Au(E_l = −1.4 V, PW = 1.0 s). Thus, these conditions were scaled up to cm^2-scale electrodes and employed in flow-electrolysis setups. We also performed flow-electrolysis studies on a planar Au (sputtered) electrode as a benchmark. A detailed discussion regarding the flow-electrolysis setup, high-performance liquid chromatography (HPLC) measurements, and Faradaic efficiency calculations can be found in the Materials and Methods Section.

Similar to our screening methodology using IAEs, we electrochemically conditioned our electrodes in 0.1 M Glycerol + 1.0 M KOH and recorded CVs at 0.1 V/s to identify potentials of interest (Figure 7b). CAs were subsequently performed for 240.0 s at these selected potentials (Figure S23a−c), and the liquid samples were collected for HPLC measurements (Figure S23d−f). Product concentrations were quantified using these chromatographs by performing calibration curves for each product (Figure S24). We also performed similar flow experiments in 0.02 M Glycerol +1.0 M KOH to study product speciation and Echem performance under the same conditions as in IAE screening experiments (Figure S25).

While the I_f and V_f measurements from CVs under flow conditions do not exactly match the values from screening experiments, this is expected as IR-drop and complex mass transport of glycerol species manifest at these large-scale electrodes due to increased size and convection due to flow, respectively. However, as seen in Figure 7b,7c, the trends in catalytic performance do translate. Like the screening experiments, even under flow conditions, Au(E_l = −1.4 V, PW = 1.0 s) achieves higher I_f at a lower V_f value than Au(E_l = −0.6 V). However, it is noteworthy that the planar Au outperforms the Au(E_l = −0.6 V, PW = 0.2 s) electrode, indicating a poor translatability of this deposition condition to practical scales. $J-V$ curves also bolster these observations (Figure 7c). Upon comparing average current density (J_{avg}) at a fixed E (1.2 V vs RHE), Au(E_l = −1.4 V, PW = 1.0 s) achieves J_{avg} of −49.5 mA/cm^2, significantly larger than J_{avg} for Au(E_l = −0.6 V, PW = 0.2 s) and planar Au, which were −13.0 and −19.1 mA/cm^2, respectively, thus showing the value of our exploration in identifying truly robust Edep conditions for electrocatalysis. From Figure 7d, it is evident that the product yield is also higher in the case of Au(E_l = −1.4 V, PW = 1.0 s), as compared to Au(E_l = −0.6 V, PW = 0.2 s) and planar Au, in line with J_{avg} measurements as shown in Figure 7c. A more detailed potential-dependent product speciation study is found in Figures S26 and S27.

Correlating product speciation trends to the nature of the gold electrode, we observed a notable difference: lower Faradaic efficiency (FE) contributions (Figure 7e) toward glyceric acid and higher combined contributions toward glycolic and formic acids in both the electrodeposited samples compared to the planar gold electrode. This difference is expected, as glyceric acid (4e$^-$ transfer step) is a C3 product formed simply via oxidation of glycerol's terminal OH group, while formic (C1) and glycolic (C2) acids are formed by further oxidation of glyceric acid via another 2e$^-$ transfer process. It has been commonly reported that cleavage of the C − C at the gold site is responsible for the generation of formic and glyceric acid, and this ability is often considered an indicator of catalytic activity.[40,42,66]

As illustrated in Figure S22, our deconvoluted CVs did reveal a high fraction of Au(110) and Au(111) sites on the electrodeposited samples. Furthermore, comparing XRDs of Au(E_l = −1.4 V, PW = 1.0 s) and Planar Au, Figure 7f reveals higher intensity peaks with smaller fwhms recorded at 64.6 and 81.8°, corresponding to the Au(220) and Au(222) peaks. This indicates the presence of large, well-ordered crystals with a higher fraction of Au(110) and Au(111) surface sites. These higher active sites, especially Au(110), are expected to increase the reactivity of glyceric acid to formic and glycolic acid, facilitated by enhanced OH adsorption.[59]

At lower operating potentials (~0.9 V vs RHE), the glycerol oxidation pathway proceeds mainly through a 4e$^-$ transfer process. As potential increases, glycerol undergoes further oxidation to generate formic and glyceric acid via a 5e$^-$ and 8e$^-$ transfer process, respectively. As seen in Figures S26 and S27, the production of these C2 and C1 products increases significantly with applied potential as C − C bond cleavage is accelerated at more oxidative potentials. This increase is even more pronounced in the case of Au(E_l = −1.4 V, PW = 1.0 s) than in planar Au, which further reinforces the role of these active sites generated via Edep. These flow electrolysis results highlight the apparent dependence of GEOR reactivity and product formation on the nature of the electrocatalyst, applied potentials, and concentration of glycerol as well. In the next stage of our screening methodology, we intend to further improve GEOR reactivity by exploring Au−Pd−Pt trimetallic systems[67] and increasing the methodology's efficiency by automating solution handling.[34,68]

CONCLUSIONS

In this study, we introduced a semiautomated approach using IAE devices and HardPotato for the deposition, screening, and analysis of heterogeneous electrocatalysts. Utilizing this platform, we conducted an in-depth examination of gold catalysts for glycerol electro-oxidation, demonstrating that electrodeposition parameters−particularly reduction potential (E_l) and pulse width (PW) significantly dictate catalytic performance. By rigorously optimizing these parameters, we identified optimal conditions of E_l = −1.4 V and PW = 1.0 s, which maximized activity and minimized issues like particle agglomeration, instabilities, and reproducibility inconsistencies. Notably, while establishing a direct correlation between E_l and GEOR activity, we discovered a peak-shaped relationship between PW and GEOR activity, which was particularly significant in identifying the superior electrocatalyst. Furthermore, our analysis elucidated the critical influence of specific surface facets in augmenting glycerol electro-oxidation, determined by the electrodeposition conditions. Finally, the scalability of our approach was validated by transitioning from μm-scale to cm-scale electrodes, which demonstrated enhanced product speciation and a stronger tendency for C−C bond cleavage in electrodeposited Au compared to planar Au electrodes, as evidenced by detailed product speciation studies.

ASSOCIATED CONTENT

Supporting Information

The Supporting Information is available free of charge at https://pubs.acs.org/doi/10.1021/acscatal.4c04190.

Further information regarding the microfabrication process, experimental methodology, such as electrodeposition results, electrocatalytic and other relevant electrochemical measurements, Tafel plots, SEM images, particle size analysis, flow-electrolyzer and HPLC measurements, and COMSOL Simulations (PDF)

Photomask design for IAE device, sample Python scripts employed to run electrodeposition and other relevant electrochemical measurements, Arduino code to control the multiplexer, Python scripts for data analysis of electrochemical experiments, and COMSOL Simulation Report (ZIP)

AUTHOR INFORMATION

Corresponding Author

Joaquín Rodríguez-López − *Department of Chemistry, University of Illinois Urbana−Champaign, Urbana, Illinois 61801, United States; Beckman Institute for Advanced Science and Technology, University of Illinois Urbana−Champaign, Urbana, Illinois 61801, United States;* orcid.org/0000-0003-4346-4668; Email: joaquinr@illinois.edu

Authors

Raghuram Gaddam − *Department of Chemistry, University of Illinois Urbana−Champaign, Urbana, Illinois 61801, United States;* orcid.org/0000-0002-2746-1566

Zirui Wang − *Department of Chemistry, University of Illinois Urbana−Champaign, Urbana, Illinois 61801, United States;* orcid.org/0009-0008-4704-3792

Yichen Li − *Department of Chemistry, University of Illinois Urbana−Champaign, Urbana, Illinois 61801, United States;* orcid.org/0009-0008-3935-0194

Lauren C. Harris − *Department of Chemistry, University of Illinois Urbana−Champaign, Urbana, Illinois 61801, United States*

Michael A. Pence − *Department of Chemistry, University of Illinois Urbana−Champaign, Urbana, Illinois 61801, United States;* orcid.org/0000-0001-5880-9812

Efren R. Guerrero − *Department of Chemistry, University of Illinois Urbana−Champaign, Urbana, Illinois 61801, United States*

Paul J. A. Kenis − *Department of Chemical and Biomolecular Engineering, University of Illinois Urbana−Champaign, Urbana, Illinois 61801, United States;* orcid.org/0000-0001-7348-0381

Andrew A. Gewirth − *Department of Chemistry, University of Illinois Urbana−Champaign, Urbana, Illinois 61801, United States;* orcid.org/0000-0003-4400-9907

Complete contact information is available at:
https://pubs.acs.org/10.1021/acscatal.4c04190

Author Contributions

All authors provided significant contributions to this work in various ways. J.R.L. conceived the project, and R.G. designed the methodology, conducted experiments, performed data analysis, and wrote the paper. Z.W. performed the microfabrication of IAE device arrays. Y.L. and E.R.G. assisted in electrodeposition experiments and electrocatalytic measurements. Y.L. also assisted in SEM image acquisition and XRD measurements. L.C.H. assisted in flow-electrolyzer experiments and the acquisition of HPLC data. M.A.P. assisted in the design of experiments and microfabrication of IAE devices. P.J.A.K., A.A.G., and J.R.L. provided supervision, oversaw project administration, acquired funding for the project, and contributed to the discussion. All authors have given approval to the final version of the manuscript.

Funding

This material is based upon the work supported by the National Science Foundation under the EFRI DCheM program Grant No. 2029326.

Notes

The authors declare no competing financial interest.

■ ACKNOWLEDGMENTS

The IAE device microfabrication was performed using the facilities and tools in the Micro-Nano-Mechanical Systems Cleanroom Laboratory, Department of Mechanical Science and Engineering at the University of Illinois. We want to thank Joseph Maduzia and Glennys Mensing for their assistance and discussions regarding the microfabrication processes. The SEM analysis was performed in the Microscopy Suite at the Beckman Institute for Advanced Sciences and Technology. We want to thank Cate Wallace for her assistance with instrument training and image acquisition. XRD measurements were taken at the George L. Clark X-ray Facility & 3 M Laboratory at the School of Chemical Sciences. We would also like to thank Rachel N. Gaines, Emiliana R. Cofell, and Saket S. Bhargava for their assistance with HPLC instrumentation, flow-electrolyzer supplies, and operation.

■ REFERENCES

(1) He, Z.; Hwang, J.; Gong, Z.; Zhou, M.; Zhang, N.; Kang, X.; Han, J. W.; Chen, Y. Promoting biomass electrooxidation via modulating proton and oxygen anion deintercalation in hydroxide. *Nat. Commun.* **2022**, *13* (1), No. 3777.

(2) Tang, C.; Zheng, Y.; Jaroniec, M.; Qiao, S.-Z. Electrocatalytic Refinery for Sustainable Production of Fuels and Chemicals. *Angew. Chem., Int. Ed.* **2021**, *60* (36), 19572−19590.

(3) Seh, Z. W.; Kibsgaard, J.; Dickens, C. F.; Chorkendorff, I.; Nørskov, J. K.; Jaramillo, T. F. Combining theory and experiment in electrocatalysis: Insights into materials design. *Science* **2017**, *355* (6321), No. eaad4998.

(4) Lucas, F. W. S.; Grim, R. G.; Tacey, S. A.; Downes, C. A.; Hasse, J.; Roman, A. M.; Farberow, C. A.; Schaidle, J. A.; Holewinski, A. Electrochemical Routes for the Valorization of Biomass-Derived Feedstocks: From Chemistry to Application. *ACS Energy Lett.* **2021**, *6* (4), 1205−1270.

(5) Werpy, T. A.; Holladay, J. E.; White, J. F. *Top Value Added Chemicals From Biomass: I. Results of Screening for Potential Candidates from Sugars and Synthesis Gas* OSTI.GOV: United States; 2004.

(6) Goetz, M. K.; Bender, M. T.; Choi, K.-S. Predictive control of selective secondary alcohol oxidation of glycerol on NiOOH. *Nat. Commun.* **2022**, *13* (1), No. 5848.

(7) Simões, M.; Baranton, S.; Coutanceau, C. Electrochemical Valorisation of Glycerol. *ChemSusChem* **2012**, *5* (11), 2106−2124.

(8) Luo, H.; Yukuhiro, V. Y.; Fernández, P. S.; Feng, J.; Thompson, P.; Rao, R. R.; Cai, R.; Favero, S.; Haigh, S. J.; Durrant, J. R.; Stephens, I. E. L.; Titirici, M.-M. Role of Ni in PtNi Bimetallic Electrocatalysts for Hydrogen and Value-Added Chemicals Coproduction via Glycerol Electrooxidation. *ACS Catal.* **2022**, *12* (23), 14492−14506.

(9) Xin, L.; Zhang, Z.; Wang, Z.; Li, W. Simultaneous Generation of Mesoxalic Acid and Electricity from Glycerol on a Gold Anode Catalyst in Anion-Exchange Membrane Fuel Cells. *ChemCatChem* **2012**, *4* (8), 1105−1114.

(10) Goetz, M. K.; Usman, E.; Choi, K.-S. Understanding and Suppressing C−C Cleavage during Glycerol Oxidation for C3 Chemical Production. *ACS Catal.* **2023**, *13* (24), 15758−15769.

(11) Yan, H.; Shen, Q.; Sun, Y.; Zhao, S.; Lu, R.; Gong, M.; Liu, Y.; Zhou, X.; Jin, X.; Feng, X.; Chen, X.; Chen, D.; Yang, C. Tailoring Facets of α-Mn2O3Microcrystalline Catalysts for Enhanced Selective Oxidation of Glycerol to Glycolic Acid. *ACS Catal.* **2021**, *11* (11), 6371−6383.

(12) Morales, D. M.; Jambrec, D.; Kazakova, M. A.; Braun, M.; Sikdar, N.; Koul, A.; Brix, A. C.; Seisel, S.; Andronescu, C.; Schuhmann, W. Electrocatalytic Conversion of Glycerol to Oxalate on Ni Oxide Nanoparticles-Modified Oxidized Multiwalled Carbon Nanotubes. *ACS Catal.* **2022**, *12* (2), 982−992.

(13) Luo, H.; Barrio, J.; Sunny, N.; Li, A.; Steier, L.; Shah, N.; Stephens, I. E. L.; Titirici, M.-M. Progress and Perspectives in Photo- and Electrochemical-Oxidation of Biomass for Sustainable Chemicals and Hydrogen Production. *Adv. Energy Mater.* **2021**, *11* (43), No. 2101180.

(14) Bagger, A.; Ju, W.; Varela, A. S.; Strasser, P.; Rossmeisl, J. Electrochemical CO2 Reduction: A Classification Problem. *ChemPhysChem* **2017**, *18* (22), 3266−3273.

(15) Wang, T.; Cao, X.; Jiao, L. Progress in Hydrogen Production Coupled with Electrochemical Oxidation of Small Molecules. *Angew. Chem.* **2022**, *134* (51), No. e202213328.

(16) Verma, S.; Lu, S.; Kenis, P. J. A. Co-electrolysis of CO2 and glycerol as a pathway to carbon chemicals with improved

technoeconomics due to low electricity consumption. *Nat. Energy* **2019**, *4* (6), 466−474.

(17) Meng, F.; Wu, Q.; Elouarzaki, K.; Luo, S.; Sun, Y.; Dai, C.; Xi, S.; Chen, Y.; Lin, X.; Fang, M.; Wang, X.; Mandler, D.; Xu, Z. J. Essential role of lattice oxygen in methanol electrochemical refinery toward formate. *Sci. Adv.* **2023**, *9* (34), No. eadh9487.

(18) Yadegari, H.; Ozden, A.; Alkayyali, T.; Soni, V.; Thevenon, A.; Rosas-Hernández, A.; Agapie, T.; Peters, J. C.; Sargent, E. H.; Sinton, D. Glycerol Oxidation Pairs with Carbon Monoxide Reduction for Low-Voltage Generation of C2 and C3 Product Streams. *ACS Energy Lett.* **2021**, *6* (10), 3538−3544.

(19) Na, J.; Seo, B.; Kim, J.; Lee, C. W.; Lee, H.; Hwang, Y. J.; Min, B. K.; Lee, D. K.; Oh, H.-S.; Lee, U. General technoeconomic analysis for electrochemical coproduction coupling carbon dioxide reduction with organic oxidation. *Nat. Commun.* **2019**, *10* (1), No. 5193.

(20) Carmo, M.; Fritz, D. L.; Mergel, J.; Stolten, D. A comprehensive review on PEM water electrolysis. *Int. J. Hydrogen Energy* **2013**, *38* (12), 4901−4934.

(21) Qian, Q.; He, X.; Li, Z.; Chen, Y.; Feng, Y.; Cheng, M.; Zhang, H.; Wang, W.; Xiao, C.; Zhang, G.; Xie, Y. Electrochemical Biomass Upgrading Coupled with Hydrogen Production under Industrial-Level Current Density. *Adv. Mater.* **2023**, *35* (25), No. 2300935.

(22) Houache, M. S. E.; Hughes, K.; Baranova, E. A. Study on catalyst selection for electrochemical valorization of glycerol. *Sustainable Energy Fuels* **2019**, *3* (8), 1892−1915.

(23) Ramprasad, R.; Batra, R.; Pilania, G.; Mannodi-Kanakkithodi, A.; Kim, C. Machine learning in materials informatics: recent applications and prospects. *npj Comput. Mater.* **2017**, *3* (1), No. 54.

(24) Fosdick, S. E.; Berglund, S. P.; Mullins, C. B.; Crooks, R. M. Evaluating Electrocatalysts for the Hydrogen Evolution Reaction Using Bipolar Electrode Arrays: Bi- and Trimetallic Combinations of Co, Fe, Ni, Mo, and W. *ACS Catal.* **2014**, *4* (5), 1332−1339.

(25) Mayer, F. D.; Hosseini-Benhangi, P.; Sánchez-Sánchez, C. M.; Asselin, E.; Gyenge, E. L. Scanning electrochemical microscopy screening of CO2 electroreduction activities and product selectivities of catalyst arrays. *Commun. Chem.* **2020**, *3* (1), No. 155.

(26) Zhao, Y.; Adams, J. S.; Baby, A.; Kromer, M. L.; Flaherty, D. W.; Rodríguez-López, J. Electrochemical Screening of Au/Pt Catalysts for the Thermocatalytic Synthesis of Hydrogen Peroxide Based on Their Oxygen Reduction and Hydrogen Oxidation Activities Probed via Voltammetric Scanning Electrochemical Microscopy. *ACS Sustainable Chem. Eng.* **2022**, *10* (51), 17207−17220.

(27) Minguzzi, A.; Alpuche-Aviles, M. A.; López, J. R.; Rondinini, S.; Bard, A. J. Screening of Oxygen Evolution Electrocatalysts by Scanning Electrochemical Microscopy Using a Shielded Tip Approach. *Anal. Chem.* **2008**, *80* (11), 4055−4064.

(28) Jung, C.; Sánchez-Sánchez, C. M.; Lin, C.-L.; Rodríguez-López, J.; Bard, A. J. Electrocatalytic Activity of Pd−Co Bimetallic Mixtures for Formic Acid Oxidation Studied by Scanning Electrochemical Microscopy. *Anal. Chem.* **2009**, *81* (16), 7003−7008.

(29) Hitt, J. L.; Li, Y. C.; Tao, S.; Yan, Z.; Gao, Y.; Billinge, S. J. L.; Mallouk, T. E. A high throughput optical method for studying compositional effects in electrocatalysts for CO2 reduction. *Nat. Commun.* **2021**, *12* (1), No. 1114.

(30) Xiang, C.; Suram, S. K.; Haber, J. A.; Guevarra, D. W.; Soedarmadji, E.; Jin, J.; Gregoire, J. M. High-Throughput Bubble Screening Method for Combinatorial Discovery of Electrocatalysts for Water Splitting. *ACS Comb. Sci.* **2014**, *16* (2), 47−52.

(31) Gerroll, B. H. R.; Kulesa, K. M.; Ault, C. A.; Baker, L. A. Legion: An Instrument for High-Throughput Electrochemistry. *ACS Meas. Sci. Au* **2023**, *3* (5), 371−379.

(32) Kulesa, K. M.; Hirtzel, E. A.; Nguyen, V. T.; Freitas, D. P.; Edwards, M. E.; Yan, X.; Baker, L. A. Interfacing High-Throughput Electrosynthesis and Mass Spectrometric Analysis of Azines. *Anal. Chem.* **2024**, *96*, 8249−8253, DOI: 10.1021/acs.analchem.4c01110.

(33) Rodríguez, O.; Pence, M. A.; Rodríguez-López, J. Hard Potato: A Python Library to Control Commercial Potentiostats and to Automate Electrochemical Experiments. *Anal. Chem.* **2023**, *95* (11), 4840−4845.

(34) Oh, I.; Pence, M. A.; Lukhanin, N. G.; Rodríguez, O.; Schroeder, C. M.; Rodríguez-López, J. The Electrolab: An open-source, modular platform for automated characterization of redox-active electrolytes. *Device* **2023**, *1* (5), No. 100103, DOI: 10.1016/j.device.2023.100103.

(35) Anitha, M.; Kamarudin, S. K.; Kofli, N. T. The potential of glycerol as a value-added commodity. *Chem. Eng. J.* **2016**, *295*, 119−130.

(36) Chen, X.; Granda-Marulanda, L. P.; McCrum, I. T.; Koper, M. T. M. How palladium inhibits CO poisoning during electrocatalytic formic acid oxidation and carbon dioxide reduction. *Nat. Commun.* **2022**, *13* (1), No. 38.

(37) Zhang, J.-h.; Liang, Y.-j.; Li, N.; Li, Z.-y.; Xu, C.-w.; Jiang, S. P. A remarkable activity of glycerol electrooxidation on gold in alkaline medium. *Electrochim. Acta* **2012**, *59*, 156−159.

(38) Budi, S.; Auliya, A.; Winarsih, S.; Fauzi, M. H.; Yusmaniar. Square-wave pulse electrodeposition of gold nanoparticles for ethanol electrooxidation. *Mater. Adv.* **2023**, *4* (22), 5556−5563.

(39) Bard, A. J.; Faulkner, L. R.; White, H. S. *Electrochemical Methods: Fundamentals and Applications*; John Wiley & Sons, 2022.

(40) Gaines, R. N.; Kleimenhagen, B. A.; Griebler, J. J.; Harris, L. C.; Gewirth, A. A.; Rogers, S. A.; Kenis, P. J. A. Optimizing the Flow Electrooxidation of Glycerol Using Statistical Design of Experiments. *J. Electrochem. Soc.* **2024**, *171* (6), No. 063506.

(41) Pence, M. A.; Rodríguez, O.; Lukhanin, N. G.; Schroeder, C. M.; Rodríguez-López, J. Automated Measurement of Electrogenerated Redox Species Degradation Using Multiplexed Interdigitated Electrode Arrays. *ACS Meas. Sci. Au* **2023**, *3* (1), 62−72.

(42) Kwon, Y.; Koper, M. T. M. Combining Voltammetry with HPLC: Application to Electro-Oxidation of Glycerol. *Anal. Chem.* **2010**, *82* (13), 5420−5424.

(43) Gomes, J. F.; Tremiliosi-Filho, G. Spectroscopic Studies of the Glycerol Electro-Oxidation on Polycrystalline Au and Pt Surfaces in Acidic and Alkaline Media. *Electrocatalysis* **2011**, *2* (2), 96−105.

(44) Fu, X.; Wan, C.; Huang, Y.; Duan, X. Noble Metal Based Electrocatalysts for Alcohol Oxidation Reactions in Alkaline Media. *Adv. Funct. Mater.* **2022**, *32* (11), No. 2106401.

(45) Rodriguez, P.; Kwon, Y.; Koper, M. T. M. The promoting effect of adsorbed carbon monoxide on the oxidation of alcohols on a gold catalyst. *Nat. Chem.* **2012**, *4* (3), 177−182.

(46) Zhang, Y.; Wang, J.-G.; Yu, X.; Baer, D. R.; Zhao, Y.; Mao, L.; Wang, F.; Zhu, Z. Potential-Dynamic Surface Chemistry Controls the Electrocatalytic Processes of Ethanol Oxidation on Gold Surfaces. *ACS Energy Lett.* **2019**, *4* (1), 215−221.

(47) Yang, L.-K.; Huang, T.-X.; Zeng, Z.-C.; Li, M.-H.; Wang, X.; Yang, F.-Z.; Ren, B. Rational fabrication of a gold-coated AFM TERS tip by pulsed electrodeposition. *Nanoscale* **2015**, *7* (43), 18225−18231.

(48) Tian, N.; Zhou, Z.-Y.; Yu, N.-F.; Wang, L.-Y.; Sun, S.-G. Direct Electrodeposition of Tetrahexahedral Pd Nanocrystals with High-Index Facets and High Catalytic Activity for Ethanol Electrooxidation. *J. Am. Chem. Soc.* **2010**, *132* (22), 7580−7581.

(49) Ye, W.; Yan, J.; Ye, Q.; Zhou, F. Template-Free and Direct Electrochemical Deposition of Hierarchical Dendritic Gold Micro-structures: Growth and Their Multiple Applications. *J. Phys. Chem. C* **2010**, *114* (37), 15617−15624.

(50) Redmond, P. L.; Hallock, A. J.; Brus, L. E. Electrochemical Ostwald Ripening of Colloidal Ag Particles on Conductive Substrates. *Nano Lett.* **2005**, *5* (1), 131−135.

(51) Łukaszewski, M.; Soszko, M.; Czerwiński, A. Electrochemical Methods of Real Surface Area Determination of Noble Metal Electrodes − an Overview. *Int. J. Electrochem. Sci.* **2016**, *11* (6), 4442−4469.

(52) Ahrens, P.; Zander, M.; Hasse, U.; Wulff, H.; Jeyabharathi, C.; Kruth, A.; Scholz, F. Electrochemical Formation of Gold Nano-particles on Polycrystalline Gold Electrodes during Prolonged Potential Cycling. *ChemElectroChem* **2018**, *5* (6), 943−957.

(53) Personick, M. L.; Jallow, A. A.; Halford, G. C.; Baker, L. A. Nanomaterials Synthesis Discovery via Parallel Electrochemical Deposition. *Chem. Mater.* **2024**, *36* (6), 3034−3041.
(54) Plowman, B. J.; Jones, L. A.; Bhargava, S. K. Building with bubbles: the formation of high surface area honeycomb-like films via hydrogen bubble templated electrodeposition. *Chem. Commun.* **2015**, *51* (21), 4331−4346.
(55) Suzuki, N. Y.; Santiago, P. V. B.; Galhardo, T. S.; Carvalho, W. A.; Souza-Garcia, J.; Angelucci, C. A. Insights of glycerol electro-oxidation on polycrystalline silver electrode. *J. Electroanal. Chem.* **2016**, *780*, 391−395.
(56) Zhang, Z.; Xin, L.; Li, W. Supported gold nanoparticles as anode catalyst for anion-exchange membrane-direct glycerol fuel cell (AEM-DGFC). *Int. J. Hydrogen Energy* **2012**, *37* (11), 9393−9401.
(57) Etesami, M.; Mohamed, N. Catalytic Application of Gold Nanoparticles Electrodeposited by Fast Scan Cyclic Voltammetry to Glycerol Electrooxidation in Alkaline Electrolyte. *Int. J. Electrochem. Sci.* **2011**, *6* (10), 4676−4689.
(58) Plaza-Mayoral, E.; Pereira, I. J.; Dalby, K. N.; Jensen, K. D.; Chorkendorff, I.; Falsig, H.; Sebastián-Pascual, P.; Escudero-Escribano, M. Pd−Au Nanostructured Electrocatalysts with Tunable Compositions for Formic Acid Oxidation. *ACS Appl. Energy Mater.* **2022**, *5* (9), 10632−10644.
(59) Kim, D.; Oh, L. S.; Tan, Y. C.; Song, H.; Kim, H. J.; Oh, J. Enhancing Glycerol Conversion and Selectivity toward Glycolic Acid via Precise Nanostructuring of Electrocatalysts. *ACS Catal.* **2021**, *11* (24), 14926−14931.
(60) Wang, Z.; Liu, P.; Han, J.; Cheng, C.; Ning, S.; Hirata, A.; Fujita, T.; Chen, M. Engineering the internal surfaces of three-dimensional nanoporous catalysts by surfactant-modified dealloying. *Nat. Commun.* **2017**, *8* (1), No. 1066.
(61) Padayachee, D.; Golovko, V.; Ingham, B.; Marshall, A. T. Influence of particle size on the electrocatalytic oxidation of glycerol over carbon-supported gold nanoparticles. *Electrochim. Acta* **2014**, *120*, 398−407.
(62) Mou, H.; Lu, F.; Zhuang, Z.; Chang, Q.; Zhang, L.; Chen, X.; Zhang, Y.; Chen, J. G. Glycerol Electrooxidation over Precision-Synthesized Gold Nanocrystals with Different Surface Facets. *Precis. Chem.* **2024**, *2* (3), 103−111.
(63) Beyhan, S.; Uosaki, K.; Feliu, J. M.; Herrero, E. Electrochemical and in situ FTIR studies of ethanol adsorption and oxidation on gold single crystal electrodes in alkaline media. *J. Electroanal. Chem.* **2013**, *707*, 89−94.
(64) Han, X.; Sheng, H.; Yu, C.; Walker, T. W.; Huber, G. W.; Qiu, J.; Jin, S. Electrocatalytic Oxidation of Glycerol to Formic Acid by CuCo2O4 Spinel Oxide Nanostructure Catalysts. *ACS Catal.* **2020**, *10* (12), 6741−6752.
(65) Kormányos, A.; Szirmai, A.; Endrődi, B.; Janáky, C. Stable Operation of Paired CO2 Reduction/Glycerol Oxidation at High Current Density. *ACS Catal.* **2024**, *14* (9), 6503−6512.
(66) Xie, Y.; Sun, L.; Pan, X.; Zhou, Z.; Zheng, Y.; Yang, X.; Zhao, G. Carbon paper supported gold nanoflowers for tunable glycerol electrooxidation boosting efficient hydrogen evolution. *Carbon* **2023**, *203*, 88−96.
(67) Yang, X.; Wang, Q.; Qing, S.; Gao, Z.; Tong, X.; Yang, N. Modulating Electronic Structure of an Au-Nanorod-Core−PdPt-Alloy-Shell Catalyst for Efficient Alcohol Electro-Oxidation. *Adv. Energy Mater.* **2021**, *11* (26), No. 2100812.
(68) Sheng, H.; Sun, J.; Rodríguez, O.; Hoar, B. B.; Zhang, W.; Xiang, D.; Tang, T.; Hazra, A.; Min, D. S.; Doyle, A. G.; Sigman, M. S.; Costentin, C.; Gu, Q.; Rodríguez-López, J.; Liu, C. Autonomous closed-loop mechanistic investigation of molecular electrochemistry via automation. *Nat. Commun.* **2024**, *15* (1), No. 2781.

https://doi.org/10.1021/acscatal.4c04190
ACS Catal. 2025, 15, 639−652